# Extention of SU2 CFD capabilities to 3D aircraft icing simulation

Kevin Ignatowicz, François Morency, Héloïse Beaugendre

**Proceedings of the 29th Annual Conference of the Computational Fluid Dynamics Society of Canada**
**CFDSC2021**
**July 27-29, 2021, Online**

# EXTENSION OF SU2 CFD CAPABILITIES TO 3D AIRCRAFT ICING SIMULATION

*Kevin Ignatowicz, François Morency*
Mechanical Engineering Department
École de technologie supérieure
Montréal, Canada
kevin.ignatowicz.1@ens.etsmtl.ca
francois.morency@etsmtl.ca

*Héloïse Beaugendre*
INRIA, CNRS
University of Bordeaux
Talence, France
heloise.beaugendre@math.u-bordeaux.fr

***Abstract***— Atmospheric icing can cause up to 16% of weather-related aircraft accidents. Ice accretions on an aircraft lead to a decrease of the aerodynamic performance and can obstruct critical sensors. Predicting the ice accretion location and shape can allow to efficiently fight against it. During the past two decades, numerical simulation of aircraft icing became a powerful complementary tool to experimental measurements. Most of the icing codes rely on the coupling between the air solution provided by CFD, a droplet solver to estimate the impingement on the geometry, and an ice accretion solver. The ice accretion solver often uses the Messinger approaches to compute the ice growth, but other numerical methods have emerged, such as the shallow water icing model (SWIM). The objective of the paper is to extend the capabilities of the open-source SU2 CFD software to ice accretion simulations by implementing the SWIM model and to verify the rime ice shape predictions. After a presentation of the model equations and implementation, the 3D results of ice accretion for the test cases NASA27 and NASA28 around a NACA0012 wing will be shown and compared to existing literature.

***Aircraft icing; Shallow water icing model; CFD; 3D icing simulation***

## I. INTRODUCTION

In-flight icing represents one of the major weather-related threats in aeronautics [1]. Several fatalities occurred following ice accretion on the aerodynamic surfaces or on sensors such as the pitot tubes, as for the Rio-Paris AF447 crash in 2009 [2]. Aerodynamic characteristics of iced wings were extensively studied, for example by Bragg [3]. Predicting the ice accretion and the subsequent loss of performance was studied experimentally by the NASA [4]. Similar studies were carried out numerically. Mainly, ice accretions on aircraft wings increase the drag and decrease the lift and the stall angle. Reference [5], using numerical simulations, highlighted that the drag on an airfoil can be increased up to 60%. The use of numerical tools has now become very popular and is an efficient complement to the experimental tests carried out in wind tunnels. The first mathematical model and numerical method were suggested in the early 50's by Messinger [6], using the mass and energy balance equations over control volumes to compute the ice accretion. The Messinger model was then improved in the early 2000's to face new numerical challenges such as unsteadiness and shear stress driven runback water [7, 8]. Mainly 2D during the early numerical developments, 3D icing simulations quickly became mandatory to tackle complex geometries [9]. In parallel, new approaches detached from the Messinger model were proposed, like the shallow water icing model (SWIM)[10]. The SWIM model is a partial differential equation (PDE) model based on the assumption that the shear stress driven runback film has a linear velocity profile in its thickness direction, with a non-slip condition at the water-wall interface. Reference [8] made a comparison between the original Messinger model, the improved models and the SWIM model, highlighting slight differences in ice shapes predictions depending on the model used.

Ice accretion solvers are usually coupled with CFD solvers to allow the transfers of air flow data to the accretion solver. Following this requirement, it is convenient to implement an ice accretion solver into an existing CFD framework. The open-source SU2 CFD solver [11] suits well for the implementation of a PDE based icing model. SU2 CFD can solve multizone problems [12], which is required to solve the airflow in the 3D fluid domain and the icing model on the surface of the geometry, usually the wing surface.

The objective of the work is to extend the capabilities of the open-source SU2 CFD solver [11] to 3D aircraft icing using the SWIM PDE model. The model equations and numerical methods will first be presented before demonstrating the 3D capabilities in the results section, with comparisons and verification against results from the literature. A mesh study is also carried out to verify the consistency of the implementation and assess the sensitivity of the accretion to the mesh resolution.

## II. MODELS AND METHODOLOGY

This section presents the main equations of the SWIM model that are implemented into the SU2 CFD solver. In addition, the treatment of the 2D surface embedded in the 3D domain will be depicted. The resolution procedure with SU2 CFD will also be presented.

### *A. The Shallow Water Icing Model (SWIM)*

The SWIM model is a PDE system with two equations: a mass balance and an energy balance. Equation (1) presents the system of PDE.

$$\frac{\partial \boldsymbol{W}}{\partial t} + \frac{\partial \boldsymbol{F}}{\partial \boldsymbol{x}} = \boldsymbol{S} \tag{1}$$

In (1), $\boldsymbol{W}, \boldsymbol{F}$ and $\boldsymbol{S}$ represent the vector of conservative variables, the convective fluxes and the source terms, respectively. Their expressions are given by (2), (3) and (4).

$$\boldsymbol{W} = \begin{pmatrix} \rho_w h_w + \rho_i h_i \\ \rho_w h_w Cp_w \bar{T} - \rho_i h_i \left(L_{fus} - Cp_i \bar{T}\right) \end{pmatrix} \tag{2}$$

$$\boldsymbol{F} = \begin{pmatrix} \rho_w h_w \bar{\boldsymbol{u}} \\ \rho_w h_w Cp_w \bar{T} \bar{\boldsymbol{u}} \end{pmatrix} \tag{3}$$

$$\boldsymbol{S} = \begin{pmatrix} \dot{m}_{imp} - \dot{m}_{es} \\ \dot{Q}_{drop} - \dot{Q}_{es} - \dot{Q}_{rad} - \dot{Q}_{conv} \end{pmatrix} \tag{4}$$

$$\bar{\boldsymbol{u}} = \frac{h_w}{2\mu_w} \boldsymbol{\tau_{wall}} \tag{5}$$

In (2) and (3), $\rho$, $h$, $Cp$, $\bar{T}$ and $\bar{\boldsymbol{u}}$ represent the density (kg/m$^3$), the thickness (m), the specific heat at constant pressure (J/kg·K), the surface temperature (°C) and the mean runback film velocity (m/s), which is given in (5). $\mu_w$ and $\boldsymbol{\tau_{wall}}$ denote the water viscosity and the local shear stress, respectively. $L_{fus}$ is the latent heat of fusion (J/kg). In (4), $\dot{m}$ and $\dot{Q}$ are the mass and energy rates, respectively. Finally, the subscripts *w*, *i*, *imp*, *es*, *drop*, *rad* and *conv* denote the water film, the ice, the impingement quantities, the evaporation and sublimation terms, the droplets energy (impingement + kinetic), the radiation and the convection, respectively. The SWIM model equations were detailed in [8] and [10]. The source terms appearing in (4) are the same as the ones described and defined in [13] for the extended Messinger model. The three unknowns of the system are the water and ice thicknesses, and the surface temperature. In addition of the PDE system, compatibility relations are needed to close the system.

$$h_w \geq 0 \tag{6}$$

$$h_w \bar{T} \geq 0 \tag{7}$$

$$\rho_i \frac{\partial h_i}{\partial t} \geq 0 \tag{8}$$

$$\rho_i \frac{\partial h_i}{\partial t} \bar{T} \leq 0 \tag{9}$$

The ice density $\rho_i$ depends on the nature of the ice. In the glaze ice situation (i.e., coexistence of liquid film and ice), the ice density is set equal to 917 kg/m$^3$ [14]. For the rime ice (i.e., only solid ice present), several approaches emerge from the literature. Reference [13] suggests a constant rime ice density equal to 880 kg/m$^3$, whereas other authors established variable density function of the ambient conditions. Reference [14] uses the density correlation from Laforte [15] to compute the rime ice density. This correlation is given in (10).

$$\rho_{i,rime} = 917 \left(\frac{X}{X + 1.3}\right)^2 \tag{10}$$

with:

$$X = \frac{dV_\infty}{-2\bar{T}} \tag{11}$$

In (11), $d$ is the median volume diameter (μm) of the impinging water droplets and $V_\infty$ (m/s) is the freestream velocity. Another rime ice density correlation is frequently used, for example in [16], and originally suggested by Jones in [17]. This correlation is given in (12).

$$\rho_{i,rime} = 1000 \exp\left(-0.15\left(1 + \frac{6043}{X^{2.65}}\right)\right) \tag{12}$$

with:

$$X = \frac{d^{0.82} {V_\infty}^{0.59} (LWC)^{0.21}}{(10D)^{0.48} (-T_a)^{0.23}} \tag{13}$$

In (13), *LWC* is the liquid water content (g/m$^3$), *D* the airfoil leading edge diameter (m) and $T_a$ is the freestream temperature (°C). This correlation is less practical to use since it depends on the geometry through the leading edge diameter, which can be non-trivial to estimate in case of complex geometries. For the implementation in SU2, all three rime ice density evaluations were implemented (i.e. constant value, Laforte correlation and Jones correlation). The comparison between the accretions obtained with each of the rime ice density correlations will be presented in the results section.

The flux terms in the PDE system (1) are evaluated using a Roe scheme for the spatial discretization of the convective fluxes [18]. In the discretized mesh, the general expression for the flux $\boldsymbol{F_e}$ crossing an edge *e* between a point *i* and a point *j* is given in (14).

$$\boldsymbol{F_e} = \frac{1}{2}\left(\boldsymbol{F}_i + \boldsymbol{F}_j\right) \cdot \vec{n} - \frac{1}{2} |A_e| \cdot \vec{n} \cdot (\boldsymbol{W}_j - \boldsymbol{W}_i) \tag{14}$$

In (14), $\vec{n}$ is the normal vector of the edge *e*. The flux terms $\boldsymbol{F}$ and the conservative variables $\boldsymbol{W}$ with the subscript *i* and *j* are the expressions (3) and (2) evaluated at the points *i* and *j*, respectively. Finally, $A_e$ is the Roe matrix associated with the edge *e*, and its eigenvalues are $\bar{u}$ and $2\bar{u}$. $\bar{u}$ is the film velocity magnitude. The temporal integration is done using a first order explicit Euler scheme, with a time step $\Delta t$ based on the maximum eigenvalue of the matrix $A_e$. Note that there are no runback water, and thus no fluxes, in the rime ice case. In that situation there is no constraint on the time step from the model equations, but only for the accuracy of the ice growth and the coupling with the air flow.

### B. The resolution using SU2 CFD

The resolution of the SWIM PDE model is done by looping over all points on the surface and performing an implicit trial-error procedure. The procedure relies on the discretized formulation of the system (1), developed in (15) for a cell *i*.

$$\boldsymbol{W_i^{n+1}} = \boldsymbol{W_i^n} + \frac{\Delta t}{\Omega}\sum_{\boldsymbol{k}} \boldsymbol{F_k^n} + \Delta t \boldsymbol{S_i^{n+1}} \tag{15}$$

The superscripts in (15) are the time levels, and $\Omega$ the area of the $i^{th}$ surface cell. For the flux term, the sum is performed on all edges *k* surrounding the point *i*. The source term, which is constant over a control volume, is evaluated at the new time level to decrease the stiffness of the system, as recommended by [18].

There are three unknowns in the system: the water film thickness $h_w$, the ice thickness $h_i$ and the surface temperature $\bar{T}$. Since the system (15) has two equations, the trial-error procedure allows setting one of the unknowns to a known value, letting only two unknowns to evaluate. During this trial-error process, the glaze ice, the rime ice and the wet (i.e. only liquid film) regimes are successively evaluated and the compatibility relations checked, using the current and previous time step solutions. For the glaze ice case, the surface temperature $\bar{T}^{n+1}$ is set to 0°C, meaning the film and ice thicknesses can be evaluated from both equations of (15). For the rime ice case, the film thickness $h_w^{n+1}$ is set to 0 m, and the ice thickness can be evaluated from the mass balance of (15). The energy balance is then iteratively solved with a Brent method [19] to evaluate the new surface temperature $\bar{T}^{n+1}$. Finally, for the wet case, the ice thickness $h_i^{n+1}$ is set to 0 m, and the mass balance of (15) allows computing the new film thickness. Again, the energy balance is solved with the Brent method to evaluate the new surface temperature $\bar{T}^{n+1}$. To reduce the computational time required to correctly guess the new cell state, the order of the trial-error procedure is adapted depending on the old surface temperature:

- If $\bar{T}^n = 0°C$
  - 1°) Test glaze ice, and if not compatible,
  - 2°) Test rime ice, and if not compatible,
  - 3°) Test wet state.
- If $\bar{T}^n < 0°C$
  - 1°) Test rime ice, and if not compatible,
  - 2°) Test glaze ice, and if not compatible,
  - 3°) Test wet state.
- If $\bar{T}^n > 0°C$
  - 1°) Test wet case, and if not compatible,
  - 2°) Test glaze ice, and if not compatible,
  - 3°) Test rime ice.

In the three situations, if none of the three states tested are compatible, an error is triggered. After all the surface's cells are updated, the next time step is performed.

The SWIM model was developed as a new solver in the SU2 CFD 6.2.0 version of the software. The icing simulations are performed using the multizone approach: the flow field is solved in the flow zone using one of the existing flow solvers in SU2 (RANS, Euler, DDES…) and the ice accretion simulation is computed on the geometry surface, usually the wing surface. The model implementation in SU2 has two different modes. The first one performs the complete flow resolution prior to solving the ice accretion. The second relies on an existing flow solution and read it to only perform the icing simulation. The first mode will be frequently used in the future developments of multilayer icing, which require a reevaluation of the flow field between each ice layer. For this paper, the SWIM model results are obtained with the second mode.

### C. The particularity of a 3D surface with SU2

One of the main features of the SWIM model is to solve the ice equations on a surface (e.g. the wing surface). The original implementation of SU2 defines either fully 2D (surface elements) or 3D (volume elements) elements, but not surface elements in a 3D space. In addition to the implementation of the SWIM model, the adaptation of the control volume construction in SU2 was thus required.

The surface elements are either triangles or quadrilaterals. The computation of their area in a 3D space is more complex than fully 2D elements. The area *S* of a 3D triangle with vertices A, B and C is given by (16). The area of a quadrilateral element is the sum of the two triangles composing it.

$$S = \frac{1}{2}\sqrt{\begin{vmatrix} x_A & x_B & x_C \\ y_A & y_B & y_C \\ 1 & 1 & 1 \end{vmatrix}^2 + \begin{vmatrix} y_A & y_B & y_C \\ z_A & z_B & z_C \\ 1 & 1 & 1 \end{vmatrix}^2 + \begin{vmatrix} z_A & z_B & z_C \\ x_A & x_B & x_C \\ 1 & 1 & 1 \end{vmatrix}^2} \tag{16}$$

In (16), the vertical brackets denote the determinant of the three column vectors in it. Verifications tests carried out on a NACA0012 extruded wing allowed to obtain the analytical wetted area of the wing by summing all the surface elements' area computed with (16).

## III. RESULTS

This section will display the results obtained with the SWIM model implementation in SU2 CFD. At first, the test cases description will be presented. Next, the grid convergence study will be shown to assess that the accretion results are not too sensitive to the grid refinement. Next, the results obtained for the NASA27 and NASA28 test cases will be compared to the literature. Finally, the last subsection will show the effects of the rime ice density correlation on the results.

### A. Test cases description

The test cases used to verify the SWIM model implementation are the cases NASA27 and NASA28 [20]. These test cases consist of a NACA0012 airfoil in a 58.1 m/s flow field at 245.2 K (NASA27) and 253.2 K (NASA28) and an angle of attack of 4°. The chord length is 0.5334 m, giving a chord-based Reynolds number of 2.5 million. The droplet liquid water content in the air is set to 1.3 g/m$^3$, the median volume diameter of the impinging droplets is 20 µm and the exposure time is 480 s. These test cases correspond to a rime ice regime, where the ambient temperature is cold enough to growth an ice accretion without a runback liquid water film. The 3D NACA0012 mesh used is from the NASA turbulence resource [21], with $2\times65$ points on the wing surface. The visualization of the mesh features is given on Fig. 1. The first node normal to the wall is at a distance of $3\cdot10^{-6}$ m. First, the flow simulation using the RANS approach is performed, using a constant wall temperature to evaluate the surface heat flux. Then, the ice accretion solver is run on the NACA0012 surface, taking as inputs the shear stress and heat flux computed by the flow solver.

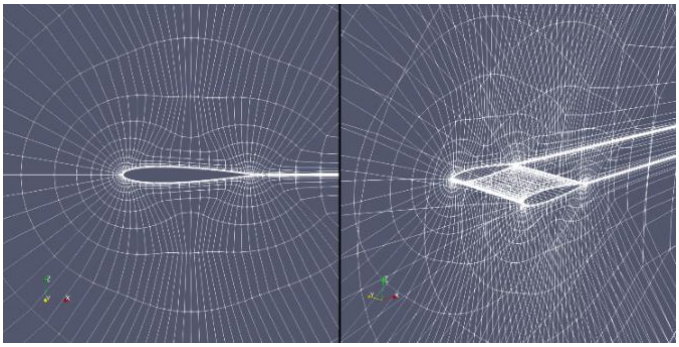

Figure 1. View of the 3D mesh used.

The surface of the wing has 64 quadrilateral elements on its surface. The collection efficiency used for the test cases is from [13] and plotted against the non-dimensional curvilinear abscissa on Fig.2. The choice of a collection efficiency from the literature removes the uncertaincy on this parameter in our verification. It ensures that the collection efficiency used in the present work and in the literature are the same. As an assumption, the impinging droplet velocity is set to the freestream velocity.

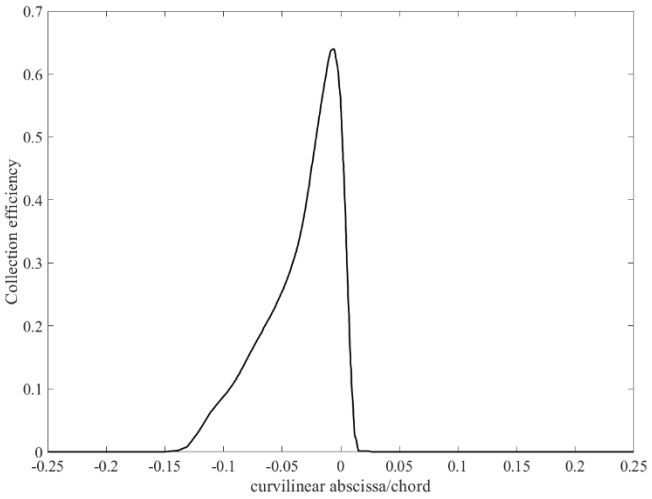


Figure 2. Collection efficiency for the NACA0012 at 4° of incidence.

It is possible to associate to each grid point its local collection efficiency by interpolating data from the graph of Fig.2. The resulting data is then used by the SWIM model as an input. The link between the collection efficiency $\beta$ and the impinging mass rate $\dot{m}_{imp}$ is given in (17).

$$\dot{m}_{imp} = LWC \times \beta \times V_\infty \tag{17}$$

The ice thicknesses computed at each surface point are used to display the deformed surface (see Fig. 3). Additionnally, the displaced points' coordinates are stored for the mesh deformation, needed for multilayer simulations.

### B. Grid study for the accretion

The grid study, relying on the methodology described by Celik [22], reports the accretion shape error related to the grid. For this purpose, three meshes were tested: a coarse with 128 cells on the wing surface, a medium with 256 cells and a fine with 512 cells. An air RANS simulation followed by an icing simulation with the ambient conditions of the case NASA28, and an exposure time of 320s were carried out on each mesh. The main accretion characteristics obtained with all three meshes are in Tab.1.

TABLE I. ACCRETION METRICS DEPENDING ON THE MESH

| Mesh | Max. thickness | Mean thickness | Iced area | Ice mass |
|---|---|---|---|---|
| Fine | 0.01840 m | 0.005674 m | 0.05165 m² | 0.2463 kg |
| Medium | 0.01839 m | 0.005616 m | 0.05221 m² | 0.2464 kg |
| Coarse | 0.01839 m | 0.005501 m | 0.05340 m² | 0.2469 kg |

Tab.1 shows that the maximum accretion thickness is almost constant and only varies with a relative error of 0.05% between the fine and the coarse meshes. For the other quantities, the values gathered in Tab.1 give the following grid convergence index (GCI) and apparent convergence order [22]:

- For the mean thickness: convergence order of 1.9 and GCI of 1.39%;
- For the iced area: convergence order of 2.2 and GCI of 1.20%;
- For the ice mass, convergence order of 5.3 and GCI of 0.008%.

The GCI highlights that the numerical uncertainty on the fine mesh for the mean thickness is 1.39%. The same analysis for the iced area and the ice mass, gives a numerical uncertainty of 1.20% and 0.008% respectively. These results are acceptable since it shows that refining the mesh doesn't cause excessive variations in the accretion metrics. Note that the variations observed in the iced area and ice mass are mainly due to the refinement of the impingement limits (through the collection efficiency, see Fig.2). Fig.3 shows a close-up on a part of the accretions to highlight the differences noted in Tab.1

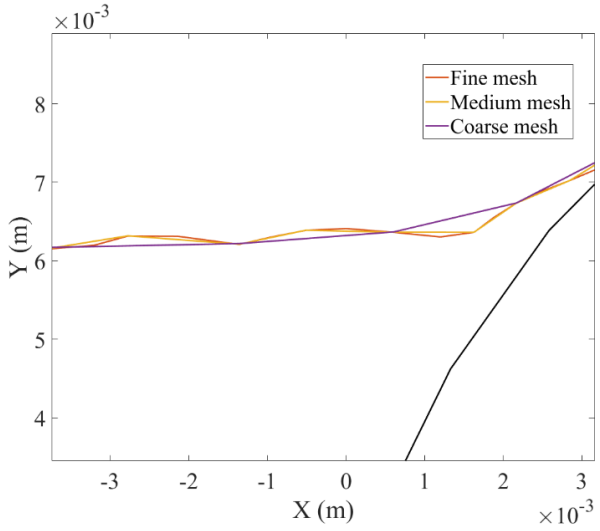


Figure 3. Close-up on the accretions obtained on different meshes.

The results show a small error that is reduced as the grid is refined, as expected. The results for the NASA27 and NASA28 test cases can be displayed and compared with the literature.

### *C. NASA27 and NASA28 test cases*

This section will present the rime ice accretion results obtained with the SWIM model implementation in SU2. The results are compared to the series of results gathered by the NASA in [20], with the software LEWICE, TRAJICE and the ONERA icing code. In addition, the experimental results are also displayed for qualitative comparison. The NASA27 and NASA28 test cases were also numerically studied by Özgen and Canibek [13] with an extended Messinger model. The literature results are 2D results on the NACA0012 airfoil. The main feature of the SU2 implementation is to be a 3D ice accretion solver. Fig. 4 allows the visualization of a 3D ice accretion obtained with SU2.

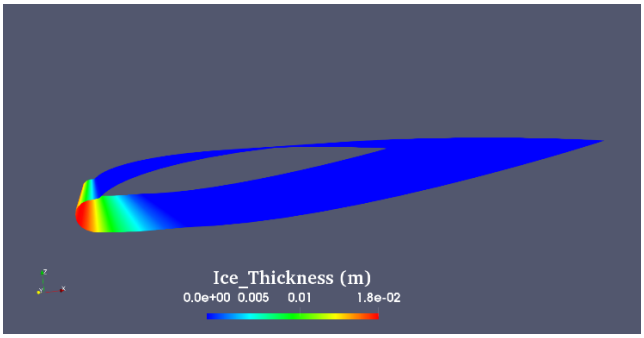


Figure 4. 3D view of the ice accretion for case NASA28. Coloring by ice thickness.

To ease comparisons with literature, a 2D cut perpendicular to the span direction is done. For the NASA27 case, Fig. 5 shows the comparison with the numerical results of [13], which were obtained using alternatively a single layer and a multilayer approcach.

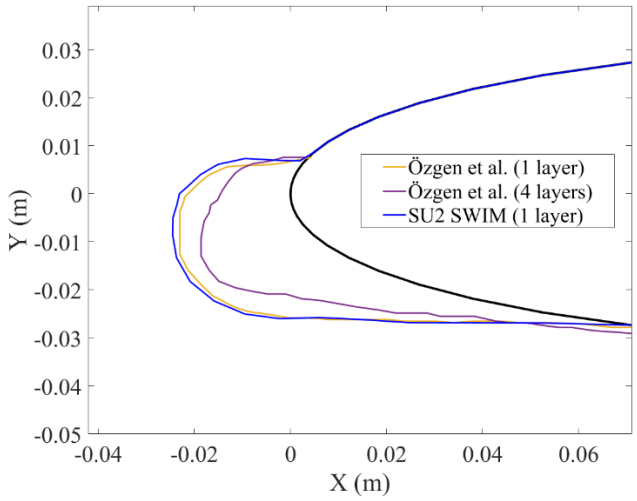


Figure 5. Comparison with the accretion of Özgen and Canibek [13], case NASA27.

Fig.5 highlights the similarities between the single layer accretion obtained by [13] and the accretion obtained with SU2 SWIM, with a slight overestimation of the thickness for the present study compared to [13]. Fig.6 displays the same NASA27 test case, but compared with the results obtained by the NASA in [20].

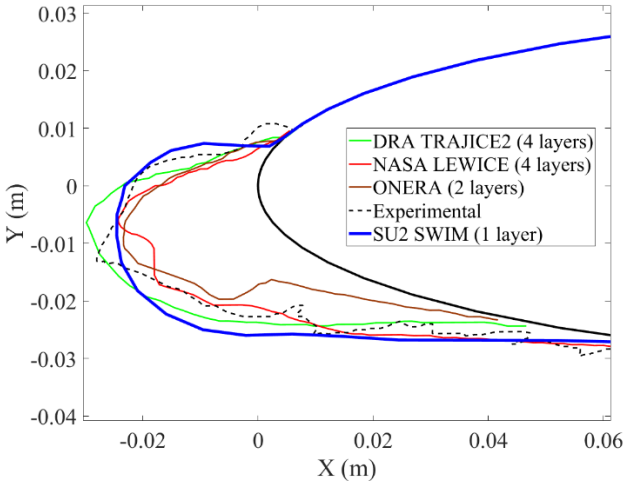


Figure 6. Comparison with the accretions from the NASA [20], case NASA27.

Fig.6 shows that the SU2 SWIM accretion is relatively close to the ice accretions dimensions published by the NASA. The main differences are due to the multilayer aspect of the results from the literature, meaning the flowfield, and most importantly the collection efficiency, are updated several times during the 480s of exposure. In the case of SU2 SWIM with a single layer, the initial collection efficiency and ice growth rate are conserved during the complete exposure time. The following Fig.7 displays the results for the NASA28 test case against [13].

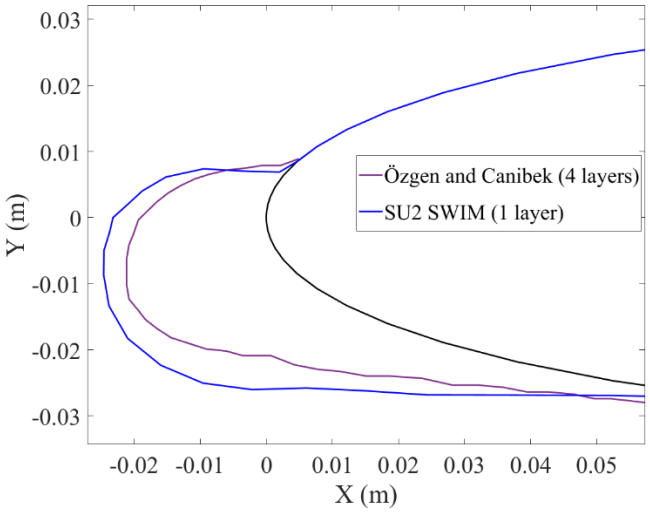


Figure 7. Comparison with the accretion of Özgen and Canibek [13], case NASA28.

Fig. 7 shows that the single layer accretion obtained with SU2 SWIM is similar in shape with the multilayer result of [13]. Fig. 8 depicts the comparison of the same SU2 SWIM accretion for the case NASA28 with the numerical and experimental results of the NASA [20].

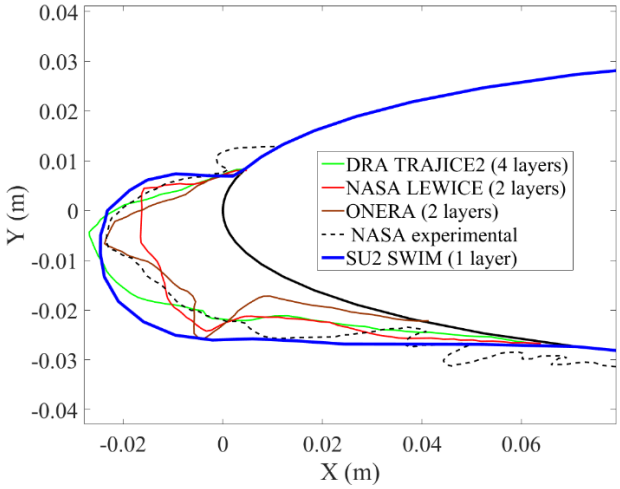


Figure 8. Comparison with the accretions from the NASA [20], case NASA28.

Fig. 8 shows a good agreement between the present accretion and the accretions in [20]: the maximum thickness and ice extension obtained with SU2 SWIM are in the same range of values, despite, again, the difference between the current single layer simulation versus the multilayer accretions for the other codes.

The validations showed that the results obtained with the SWIM model in SU2 CFD solver are in good agreement with the literature for the NASA27 and NASA28 rime ice cases. The results shown in the present section were obtained with a rime ice density set constant to 880 kg/m$^3$, following the hypothesis made by [13]. The next subsection will highlight the sensitivity of the accretion to the choice of the rime ice density correlation.

### *D. Influence of the rime density correlation*

The literature review led to the implementation of three approaches to compute the rime ice density: constant, using Jones [17] correlation or Laforte [15] correlation. Fig.9 shows the shapes differences obtained with these three correlations on an accretion after 320s of exposure.

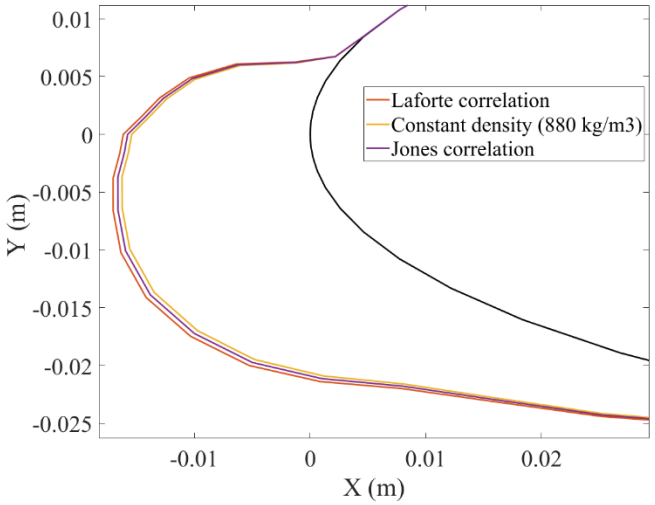


Figure 9. Comparison of the ice thicknesses according to the choice of the rime density correlation.

Fig.9 shows that Laforte correlation gives the highest thickness and Jones correlation the lowest. This is in accordance with the density computed: 840.3 kg/m$^3$ for Laforte correlation and 860.5 kg/m$^3$ for Jones correlation. The variations of thickness observed were less than 1 mm on an accretion with the maximum thickness of about 18 mm, meaning that the variations in thickness caused by the density calculation are under 5%.

## IV. CONCLUSION

The objective of extending the capabilities of SU2 CFD solver to 3D icing simulation was reached for rime ice accretion. The shallow water icing model (SWIM) is implemented and solved on the geometry surface in the 3D domain. This feature of solving a 2D problem embedded in a 3D space is a new feature in SU2. The SWIM model presents satisfactory results when compared to the literature for the test cases NASA27 and NASA28, showing less than 9% of error on the maximum ice thickness compared to the results of the NASA. In addition, it was highlighted that the ice accretions obtained evolved consistently with grid refinement and that the choice of the rime ice density impacts the ice thickness for less than 5%. Future steps will verify the glaze ice regime and extend the implementation to multilayer ice accretion simulations, including mesh deformation.

## ACKNOWLEDGMENT

The authors want to thank ÉTS Montréal and Le TOMATO association from Aéroclub de France for the support.

## REFERENCES

[1] I.A.T.A., Safety Report 2015. International Air Transport Association: Montreal, Quebec, 2016.

[2] Conversy, S., Chatty, S., Gaspard-Boulinc, H., and Vinot, J.-L., The Accident of Flight AF447 Rio-Paris: a Case Study for HCI Research, in IHM'14, 26e conférence francophone sur l'Interaction Homme-Machine. ACM: Lille, France, 2014, p. 60-69.

[3] Bragg, M.B., Broeren, A.P., and Blumenthal, L.A., Iced-airfoil aerodynamics. *Progress in Aerospace Sciences* **2005**, *41*, No. 5, 2005, p. 323-362.

[4] Shin, J. and H. Bond, T., *Results of an icing test on a NACA 0012 airfoil in the NASA Lewis Icing Research Tunnel*. 1992.

[5] Tagawa, G.D., Morency, F., and Beaugendre, H. "CFD study of airfoil lift reduction caused by ice roughness", *2018 Applied Aerodynamics Conference*, 2018.

[6] Messinger, B.L., Equilibrium Temperature of an Unheated Icing Surface as a Function of Air Speed. *Journal of the Aeronautical Sciences* **1953**, *20*, No. 1, 1953, p. 29-42.

[7] Myers, T.G., Extension to the Messinger Model for Aircraft Icing. *AIAA Journal* **2001**, *39*, No. 2, 2001, p. 211-218.

[8] Lavoie, P., Pena, D., Hoarau, Y., and Laurendeau, E., Comparison of thermodynamic models for ice accretion on airfoils. *International Journal of Numerical Methods for Heat & Fluid Flow* **2018**, *28*, No. 5, 2018, p. 1004-1030.

[9] Zhu, C., Fu, B., Sun, Z., and Zhu, C., 3D Ice Accretion Simulation For Complex Configuration Basing On Improved Messinger Model. *International Journal of Modern Physics: Conference Series* **2012**, *19*, No. 2012, p. 341-350.

[10] Bourgault, Beaugendre, and Habashi, Development of a Shallow-Water Icing Model in FENSAP-ICE. *Journal of Aircraft* **2000**, *37*, No. 4, 2000, p. 640-646.

[11] Economon, T.D., Palacios, F., Copeland, S.R., Lukaczyk, T.W., and Alonso, J.J., SU2: An Open-Source Suite for Multiphysics Simulation and Design. *AIAA Journal* **2015**, *54*, No. 3, 2015, p. 828-846.

[12] Burghardt, O., Albring, T., and Gauger, N.R., CHT problems and computing coupled discrete adjoints using AD. Chair of scientific computing , TU Kaiserslautern: Kaiserslautern, 2018.

[13] Özgen, S. and Canıbek, M., Ice accretion simulation on multi-element airfoils using extended Messinger model. *Heat and Mass Transfer* **2008**, *45*, No. 3, 2008, p. 305.

[14] Fortin, G. and Perron, J., Wind Turbine Icing and De-Icing. *AIAA Journal* **2009**, No. 2009.

[15] Laforte, J.-L. and Allaire, M.A., Évaluation du givromètre d'Hydro-Québec à différentes intensités de givrage sec et humide. Hydro-Québec, Études et Normalisation Équipement de Transport: Montréal, QC, Canada, 1992.

[16] Zhang, X. and Wu, X., Model for aircraft icing with consideration of property-variable rime ice. *International Journal of Heat and Mass Transfer* **2016**, *97*, No. 2016, p. 185-190.

[17] Jones, K.F., The density of natural ice accretions related to nondimensional icing parameters. *Quarterly Journal of the Royal Meteorological Society* **1990**, *116*, No. 492, 1990, p. 477-496.

[18] Blazek, J., *Computational Fluid Dynamics: Principles and Applications*. Second Edition ed.: Elsevier, 2005.

[19] Brent, R., Algorithms For Minimization Without Derivatives. *Englewood Cliffs, Prentice Hall* **2002**, *19*, No. 2002.

[20] Wright, W.B., Gent, R.W., and Guffond, D., DRA/NASA/ONERA Collaboration on Icing Research. Part II- Prediction of Airfoil Ice Accretion, 1997.

[21] Nasa. *Turbulence Modeling Resource*. 2013. [cited 2021]; Available from: https://turbmodels.larc.nasa.gov/naca0012_val.html.

[22] Celik, I., Ghia, U., Roache, P.J., Freitas, C., Coloman, H., and Raad, P., Procedure of Estimation and Reporting of Uncertainty Due to Discretization in CFD Applications. *J. Fluids Eng.* **2008**, *130*, No. 2008, p. 078001.